

Influence of multiband sign-changing superconductivity on vortex cores and vortex pinning in stoichiometric high- T_c $\text{CaKFe}_4\text{As}_4$

Antón Fente,¹ William R. Meier,^{2,3} Tai Kong,^{2,3} Vladimir G. Kogan,² Sergey L. Bud'ko,^{2,3} Paul C. Canfield,^{2,3} Isabel Guillamón,¹ and Hermann Suderow¹

¹*Laboratorio de Bajas Temperaturas y Altos Campos Magnéticos, Unidad Asociada UAM/CSIC, Departamento de Física de la Materia Condensada, Instituto de Ciencia de Materiales Nicolás Cabrera and Condensed Matter Physics Center (IFIMAC), Universidad Autónoma de Madrid, E-28049 Madrid, Spain*

²*Ames Laboratory, Ames, Iowa 50011, USA*

³*Department of Physics & Astronomy, Iowa State University, Ames, Iowa 50011, USA*



(Received 20 December 2017; revised manuscript received 8 March 2018; published 2 April 2018)

We use a scanning tunneling microscope to study the superconducting density of states and vortex lattice of single crystals of $\text{CaKFe}_4\text{As}_4$. This material has a critical temperature of $T_c = 35$ K, one of the highest among stoichiometric iron based superconductors (FeBSCs), and is comparable to T_c found near optimal doping in other FeBSCs. We observe quasiparticle scattering from defects with a pattern related to interband scattering between zone centered hole sheets. We measure the tunneling conductance in vortex cores and find a peak due to Caroli–de Gennes–Matricon bound states. The peak is located above the Fermi level, showing that $\text{CaKFe}_4\text{As}_4$ is a clean superconductor with vortex core bound states close to the so-called extreme quantum limit. We identify locations where the superconducting order parameter is strongly suppressed due to pair breaking. Vortices are pinned at these locations, and the length scale of the suppression of the order parameter is of order of the vortex core size. As a consequence, the vortex lattice is disordered up to 8 T.

DOI: [10.1103/PhysRevB.97.134501](https://doi.org/10.1103/PhysRevB.97.134501)

I. INTRODUCTION

The Fermi surface of iron based superconductors (FeBSC) may consist of five different sheets where the superconducting gap opens with different sizes. Sometimes gap sizes cluster around two values, leading to so-called effective two-gap superconductivity [1–6]. The highest T_c 's of FeBSC are either found in doped systems with substitutional disorder or under substantial pressure, strain, or stress, except in the recently discovered $Ae\text{AFe}_4\text{As}_4$ ($Ae = \text{Ca, Sr, Eu}$ and $A = \text{K, Rb, Cs}$) systems [7,8] where $T_c \cong 35$ K is obtained in stoichiometric compounds. This provides an outstanding opportunity to understand the main features characteristic of superconductivity in FeBSC, because there is no substitutional disorder. In addition, there is no structural nor magnetic transition, which eliminates disorder due to domains of crystalline orientations often found in FeBSC [8,9].

Penetration depth and tunneling experiments in $\text{CaKFe}_4\text{As}_4$ show evidence for two well defined superconducting gaps and sign changing behavior in agreement with s_{\pm} superconductivity [10]. Results are comparable to those in optimally doped $(\text{Ba}_{1-x}\text{K}_x)\text{Fe}_2\text{As}_2$. The band structure is also similar to that of $(\text{Ba}_{1-x}\text{K}_x)\text{Fe}_2\text{As}_2$, with three hole pockets at the Γ point and two electron pockets at the M point, having two main superconducting gap values [10,11]. Substitution of Fe in $\text{CaKFe}_4\text{As}_4$ with Ni and Co, stabilizes a hedgehog noncollinear magnetic order [12]. Nuclear magnetic resonance (NMR) experiments on pure $\text{CaKFe}_4\text{As}_4$ show spin-singlet superconductivity and no Hebel-Slichter peak, with exponentially decaying spin relaxation rates, all compatible with nodeless s_{\pm} superconductivity. Furthermore, alternating K and Ca layers are found to be well ordered and signatures of antiferromagnetic spin

fluctuations consistent with a hedgehog spin vortex crystal are also found [13]. Here we take advantage of the unique properties of $\text{CaKFe}_4\text{As}_4$ to identify relevant features of the band structure through quasiparticle scattering and to determine the influence of the spatial dependence of the superconducting density of states in the properties of vortex lattice.

We study $\text{CaKFe}_4\text{As}_4$ using cryogenic scanning tunneling microscopy (STM)—a powerful tool offering insight into the band structure and the superconducting properties, due to a high spatial and energy resolution. We first determine the gap structure in different sheets of the Fermi surface using quasiparticle interference. We then show vortex core bound states and determine the vortex core size and its magnetic field dependence. Finally, we discuss vortex pinning due to defects that suppress the order parameter at length scales of order of the vortex core size.

II. EXPERIMENT

We grew single crystals of $\text{CaKFe}_4\text{As}_4$ from a high temperature Fe-As rich melt, using As (99.9999%), K (99.95%), and Fe (99.9%) from Alfa Aesar, and Ca from Ames Laboratory Materials Preparation Center (99.9%), following the procedure described in Ref. [8]. Crystals were screened to make sure that they are single phase, as in Refs. [8,10–15], and have shiny flat surfaces. Crystals are plate-like, of several millimeters size and several hundreds of microns thick, with the c axis perpendicular to the surface. We cleaved the samples *in situ* along (001) by gluing a brass stick to the surface and removing it at 4.2 K using a movable sample holder [14,16]. After performing the experiment and warming the system, we saw that the cleaved

surface is optically shiny and flat. The base temperature of our cryogenic system was of 800 mK and we used a gold tip prepared *in situ* as described in Ref. [17]. By moving the sample holder below the tip, we can change the scanning window *in situ*. During this particular experiment, we have studied about 50 different fields of view $2 \times 2 \mu\text{m}$ in size. Magnetic fields are applied perpendicular to the surface (parallel to the c axis) using a superconducting coil (in zero-field-cooled conditions). We report the tunneling conductance normalized by its value at a bias voltage far from the superconducting features. $\text{CaKFe}_4\text{As}_4$ consists of atomically flat areas showing disordered arrangements of small size features (a few nm size). The surface looks similar to surfaces found in $(\text{Ba}_{0.6}\text{K}_{0.4})\text{Fe}_2\text{As}_2$ [18]. A detailed discussion of surface features and the observed defects is provided in the Appendix.

III. RESULTS

A. Band structure and superconducting gap

Let us first discuss tunneling conductance maps at zero magnetic field. Real space tunneling conductance maps show

wiggles and features with wavelengths larger than interatomic distances due to quasiparticle interference. By making maps with enough points in real space, we cover wave vectors in reciprocal space of order of the size of the Fermi surface pockets. We show Fourier transforms of real space conductance maps at different bias voltages in Fig. 1(a). We observe that the scattering pattern increases its size in reciprocal space when increasing the bias voltage and considerably loses intensity above the Fermi level. In addition, around the Fermi level [within the superconducting gap, see lower left panel in Fig. 1(a)], the scattering intensity strongly decreases.

The quasiparticle scattering intensity g depends on the energy E and on \vec{q} , the scattering vector from \vec{k}_1 to \vec{k}_2 ($\vec{q} = \vec{k}_2 - \vec{k}_1$). $g(E, \vec{q})$ is determined by the scattering potential V_S and the joint density of states $J(E, \vec{q})$, $g(E, \vec{q}) \propto |V_S(\vec{q})|^2 J(E, \vec{q})$. This assumes elastic scattering and neglects the energy dependence of the tunneling matrix elements and coherence effects due to superconductivity [19,20]. The joint density of states is given by $J(E, \vec{q}) \propto N_1(E, \vec{k}_1)N_2(E, \vec{k}_2)$, where N_1 and N_2 are the densities of states at \vec{k}_1 and \vec{k}_2 . $J(E, \vec{q})$ is maximal for vectors

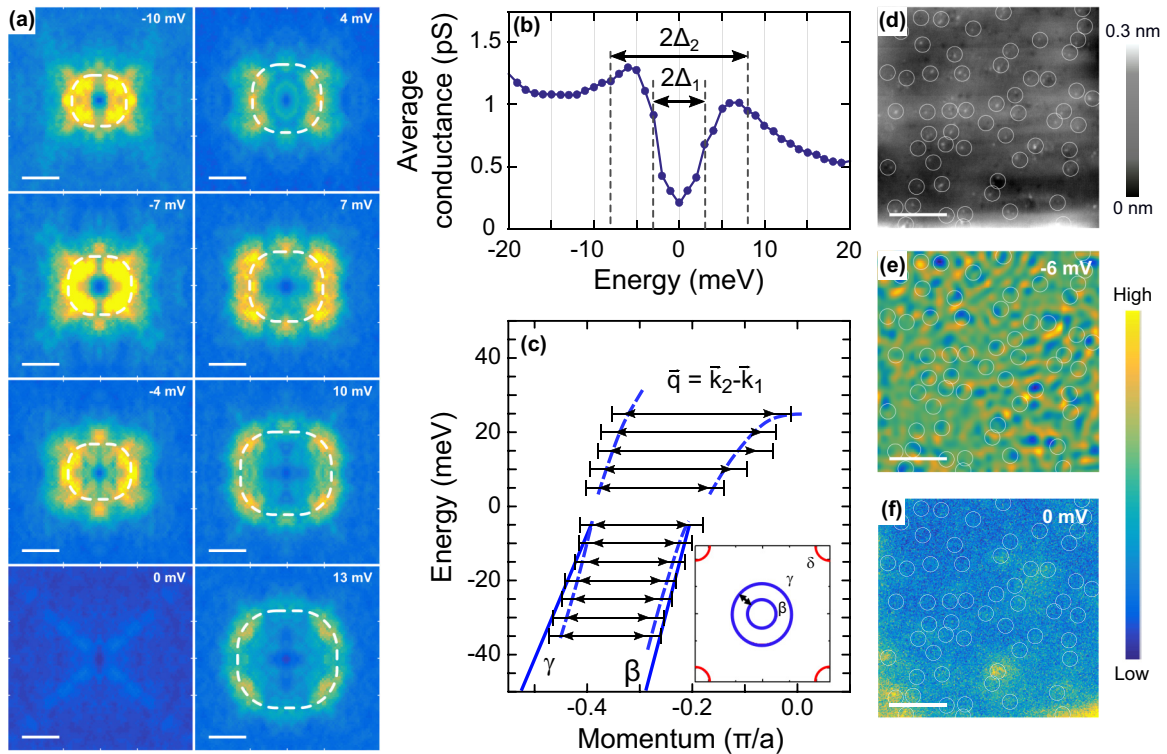


FIG. 1. (a) The Fourier transform of scattering patterns at defects at different bias voltages in zero magnetic field and 0.8 K. The white scale bar is $0.1\pi/a$ where a is the in-plane lattice parameter ($a = 3.861 \text{ \AA}$ at about 6 K, see [8]). (b) The magnitude of the Fourier transform averaged over the path marked by the white dashed lines in (a) as a function of the bias voltage. (c) The reciprocal space vector obtained from our data (black lines with arrows) as a function of the energy. The length of the black lines is the radius of the interference pattern marked in (a) by a white dashed circle. Lateral error bars provide the width of the pattern. We also plot a simplified schematics of the band dispersion obtained from angle-resolved photoemission spectroscopy (ARPES). In the main panel, ARPES data are shown as blue lines, including β hole and γ electron sheets. In the inset we show the Fermi surface, with hole sheets as blue circles and electron sheets as red circles [11]. For clarity, we do not show the α band, which is a small hole band at the center of the Brillouin zone. Our data (black lines with arrows) follow the band dispersion schematically shown by dashed blue lines in the main panel. In the inset we show the corresponding vector as a black line with arrows. (d) The real space topographic STM map (color scale bar giving height differences at the right). White circles highlight defects observed at the surface. High resolution images of defects are provided and discussed in the Appendix. (e) and (f) Tunneling conductance maps roughly at the gap edge (e) and at zero bias (f) using the same conductance scale (color bar giving conductance differences at the right). White circles are at the positions where we find defects in (d). White scale bars in (d)–(f) are of 20 nm.

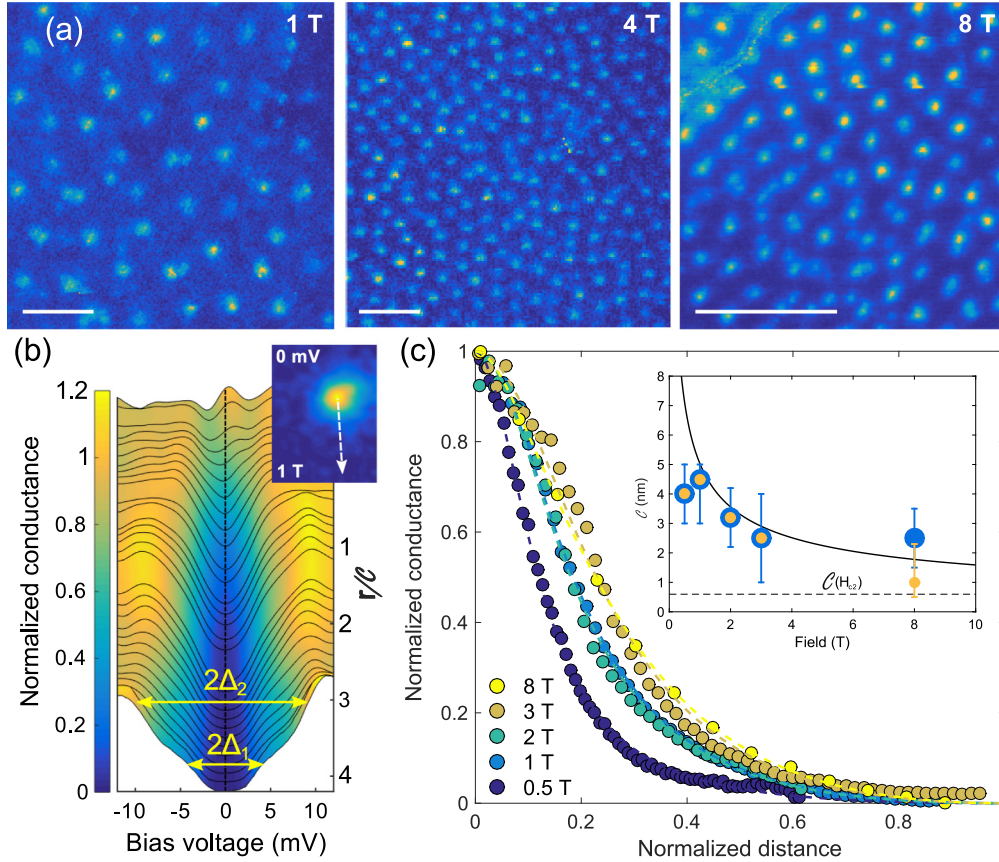


FIG. 2. (a) Zero bias tunneling conductance maps made at three different magnetic fields (1 T, left panel, 4 T, middle panel and 8 T, right panel; images are taken at different locations). White scale bars are of 82 nm size. We show more vortex lattice images together with the intervortex distance a_0 vs magnetic field in the Appendix. a_0 follows expectations for a hexagonal Abrikosov lattice. (b) The tunneling conductance vs bias voltage from the center of the vortex (top curves) to outside the vortex (bottom curves). Distance (scale bar at the right) is normalized to the vortex core size C . We mark the two values of the superconducting gap by yellow arrows. In the inset we show the zero bias conductance map at one vortex, with the path followed in the main panel marked by a white arrow. (c) The normalized conductance vs the distance normalized to the size of the Wigner Seitz unit cell of the vortex lattice for different magnetic fields. The inset shows the vortex core size (obtained as described in the text) vs the magnetic field. Dashed line shows the vortex core size extrapolated up to H_{c2} .

\vec{q} connecting two parts of the electronic dispersion on equal energy contours at the energy E (measured with respect to the Fermi level, E_F). The tunneling conductance as a function of the bias voltage V follows $g(\vec{q})$ as a function of E (with $V = 0$ for $E = E_F$). Thus, the tunneling conductance maps follow the electronic dispersion relation for filled ($V \leq 0$) and empty ($V \geq 0$) states.

The quasiparticle scattering pattern shown in Fig. 1(a) shows slight in-plane anisotropic features. Defects are in-plane asymmetric, as discussed in the Appendix. Thus, the anisotropy of the scattering pattern is due to the internal structure of defects, i.e., to an in-plane anisotropic $|V_S(\vec{q})|^2$. Probably, the joint density of states $J(E, \vec{q})$ corresponding to our quasiparticle pattern is mostly in-plane isotropic, in agreement with previous ARPES measurements [11] and with the shape of the vortex core, reported below.

The radius of the scattering pattern in the Fourier transform gives a scattering wave vector \vec{q} that is quite small. The vector \vec{q} increases with energy and therefore, if we consider intraband scattering vectors, it might correspond to an electron band. However, when we compare our result with ARPES data [11], we find that this vector is half of the size expected for the

electron intraband scattering. On the other hand, interband scattering giving such a small wave vector can involve only the hole bands at the zone center. The distance between the γ band and the β bands as measured in ARPES is the same as the size of the observed wave vector [Fig. 1(c)]. The considerable increase in \vec{q} observed for positive biases (above the Fermi level), together with the reduction of the scattering intensity point out that one of the two bands involved in scattering, namely the internal β band, reaches its top close to the Fermi level [Fig. 1(c)].

In Fig. 1(b) we show the Fourier transform of the scattering pattern averaged along the dashed line as a function of the bias voltage. This shows the energy dependence of the joint density of states, $J(E) \propto N_1(E)N_2(E)$, at the vector corresponding to the scattering between hole bands. The quasiparticle peak is located at a similar position as in previous measurements of the tunneling conductance vs bias voltage [10]. There are shoulders in the curve at the values of the superconducting gap Δ_1 and Δ_2 determined using tunneling conductance and penetration depth [10]. Thus, Δ_1 and Δ_2 both open in the hole bands surrounding the zone center. This compares well with ARPES measurements, which show the largest and smallest

gap values at, respectively, the β and γ sheets [11]. Here, in addition, we can access the empty states above the Fermi level, finding that the β band (which also carries the largest superconducting gap Δ_2 according to ARPES) has its top close to the Fermi level.

By comparing tunneling conductance with topographic images, we can discuss the relationship among different defects and the superconducting order parameter. In Fig. 1(d) we show the topographic STM image obtained at the same time as the conductance maps. We have highlighted defect positions by white circles. In Fig. 1(e) we show a representative tunneling conductance map within the gap, at $V = -6$ mV. There are modulations with large wavelength whose intensity is mostly located close to the defects highlighted by the white circles. As we discuss in detail in the Appendix, the surface consists of linear features interspersed with defects. The direction of the modulation is the same as the linear features of the topography. This provides an anisotropic scattering potential $|V_S(\vec{q})|^2$.

The zero bias conductance map [Fig. 1(f)] remains unaffected by these scattering centers. This implies that scattering between hole bands does not produce any suppression of the order parameter and shows that the gap has the same sign in the bands close to zone center. The sign changing order parameter identified using penetration depth measurements in [10] probably occurs between the band at the zone boundary and the bands at the zone center.

There are scattering centers in the same field of view that lead to a suppression of the order parameter. This provides locations with an increased zero bias conductance, as shown by the yellow blobs in the bottom part of Fig. 1(f). These areas are quite large in size (reaching several nm) and consist of blobs or lines. As we discuss below, these defects have a strong effect on vortex pinning.

B. Vortex cores

When we apply a magnetic field we observe the vortex arrangement over the whole cleaved surface [Fig. 2(a)]. Let us first focus on the shape and size of the vortex core. We show an image with an isolated vortex in the upper panel of Fig. 2(b). As can be seen there [and also in Fig. 2(a)], vortex cores are essentially round in $\text{CaKFe}_4\text{As}_4$, showing no conspicuous in-plane anisotropy. The spatial anisotropy of the vortex core is related to the in-plane anisotropy of the superconducting gap [21–25]. We find in-plane isotropic vortex cores, i.e., there is practically no anisotropy in the in-plane gap structure, in agreement with ARPES.

We show the evolution of the tunneling conductance from the vortex core to the gapped region in between vortices in the main panel of Fig. 2(b). Results are similar for all magnetic fields up to 8 T. The normalized tunneling conductance at the vortex center shows a small peak for positive bias voltages [upper curves of Fig. 2(b)]. The peak is due to quantized vortex core levels predicted by Caroli, de Gennes, and Matricon and observed in many materials [21–24]. The peak observed in $\text{CaKFe}_4\text{As}_4$ is slightly asymmetric and located at a nonzero bias. The lowest lying quantized state is located at $\frac{\Delta^2}{2E_F}$, where Δ is the superconducting gap and E_F the Fermi energy. $\frac{\Delta^2}{2E_F}$

is usually of order of a few μeV and thus nearly negligible, as E_F is often large, of order of eV, and Δ small, of order of meV. This results in a zero bias peak in the tunneling conductance in, for instance 2H-NbSe₂ or 2H-NbS₂ [22,26,27]. However, if Δ is large and/or E_F small, the vortex core state at the center of the vortex is located at a nonzero bias, as we observe here.

In Fig. 2(c) we show the size of the vortex core as a function of the magnetic field, obtained as described in [28]. The vortex core size is treated separately for each group of bands, giving different values of the superconducting gap, and is defined as $C_i \propto \Delta_{OP,Max,i} (d\Delta_{OP,i}/dr|_{r \rightarrow 0})^{-1}$, where $\Delta_{OP,i}$ is the order parameter in each band, $\Delta_{OP,Max,i}$ the maximum gap between vortices and, r the distance from the vortex center. Our fits to C_i provide the same values of C_i for each band, except at 8 T, where we obtain a difference. The extracted C_i follow the behavior expected for a superconductor in the clean limit, $C_i \propto 1/\sqrt{H}$. When we extrapolate C_i to $H_{c2} \approx 70$ T we find a value for the in-plane coherence length ξ of 0.7 nm, which is somewhat smaller, although of order of the value obtained previously from H_{c2} (1.4 nm, using $\xi \approx \sqrt{\phi_0/2\pi H_{c2}}$) [8].

C. Vortex lattice and vortex pinning

When we measure the vortex lattice, we find sixfold symmetric vortex patterns, showing that the underlying order is hexagonal over the whole magnetic field range we study (from a few hundred mT to 8 T). However, the position of vortices is strongly influenced by the order parameter suppression observed around defects. As we have shown in Fig. 1(f) at zero field, there are some locations where we observe pair breaking in form of a finite zero bias conductance. In some fields of view, these locations are not related to features in the topography [as in Fig. 1(f)], but in other fields of view they can be linked to a step on the surface. In Figs. 3(b) and 3(c) we show tunneling conductance maps taken at 2 T and at 3 T at the same location. Images show several steps producing lines with a finite zero bias conductance. Some vortices are positioned along these lines and some even form a chain along the step with a high zero bias conductance. The step might be due to a structural defect in the bulk that suppresses the order parameter. Vortices around the defect change their position when increasing the magnetic field from 2 T to 3 T, but the vortices marked by white circles remain at the same positions, along the lines with a high zero bias conductance. Thus, vortices are pinned to the locations with finite zero bias conductance. As can be seen in Figs. 3(b) and 3(c), the lateral size of the locations with pair breaking coincides with the vortex core size C_i .

In Fig. 3(d) we discuss a map showing many vortices. We have Delaunay triangulated vortex positions. The concentration of defects in the vortex lattice is very high, with roughly the same number of fivefold and sevenfold vortices, that sums up to nearly the number of vortices with six nearest neighbors [Fig. 3(f)]. The positional correlation function $G_K(r)$ [Fig. 3(e)] decays following $e^{-r/L}$ with L of 4–5 intervortex distances a_0 . We see that ordered bundles include just a few hexagons. The behavior in Figs. 3(a)–3(c) is characteristic for isolated vortex pinning, i.e., vortices are located exactly on the pinning centers. The behavior in Fig. 3(d) is characteristic

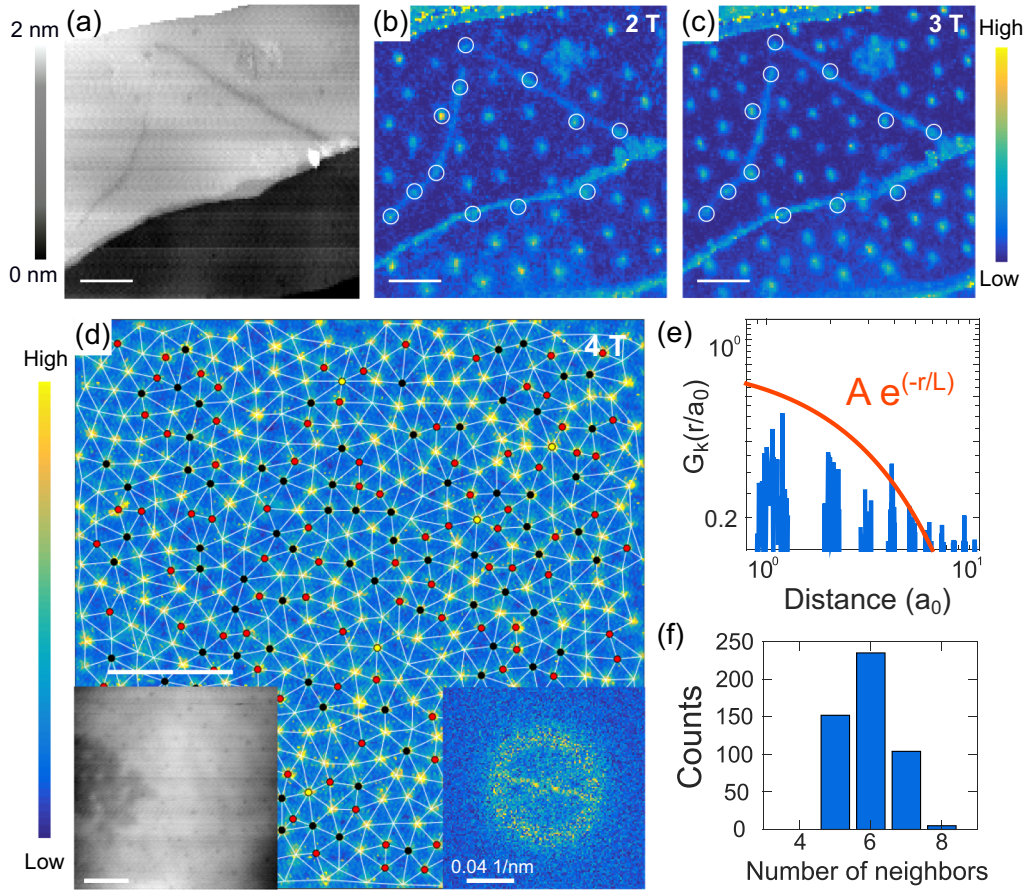


FIG. 3. (a) STM topographic image with different step edges. There is one large step from bottom left to middle right of the image and two steps at an angle to it. Height differences are given by the grey bar on the left. (b) and (c) The zero bias tunneling conductance map at this location at 2 T (b) and 3 T (c). White scale bars in (a)–(c) are of 50 nm. White circles mark the position of vortices along the steps in at 2 T. Normalized tunneling conductance scale is given by the right bar. In (d) we show a large zero bias conductance map showing a disordered vortex lattice at 4 T. Vortex positions are Delaunay triangulated (lines and colored dots). Vortices with seven nearest neighbors are marked in black, with five nearest neighbors in red, and with eight nearest neighbors in yellow. The bottom left panel shows the corresponding topographic STM image and bottom right panel the Fourier transform of the tunneling conductance image. (e) The positional correlation function vs distance in units of the intervortex distance $a_0 = \sqrt{2}\phi_0/\sqrt{3}B$ (top panel) and the histogram over the number of nearest neighbors (bottom panel).

of collective pinning, i.e., vortices distribute on a disordered hexagonal lattice, being pinned to many locations with order parameter suppression along the vortex length [29].

IV. DISCUSSION AND CONCLUSIONS

From the structural point of view, the $\text{CaKFe}_4\text{As}_4$ system is related to CaFe_2As_2 but has alternating Ca and K layers [4]. In the latter case, the Fe-As sheets are centered between the Ca planes. In $\text{CaKFe}_4\text{As}_4$ the larger K ions shift these sheets towards K and destroy the n -glide symmetry across the Fe plane present in most iron based superconductors. Moreover, the As atoms next to K and Ca become inequivalent and adopt different distances from the Fe plane. Band structure calculations in $\text{CaKFe}_4\text{As}_4$ show that the band dispersion has a much stronger two-dimensional character than in the CaFe_2As_2 and related systems, which can enhance Coulomb interactions and favor unconventional $s\pm$ superconductivity [30]. Calculations indeed show that the order parameter changing sign between electron and hole pockets is favored by antiferromagnetic spin fluctuations and Coulomb repulsion [30]. The structure of sign

changes is expected to be more intricate with less Coulomb repulsion, showing sign changes of the order parameter within hole and electron bands. Here we show that there are no sign changes within the hole bands, or otherwise the quasiparticle interference scattering we consider (Fig. 1) would lead to suppression of superconductivity.

Along the same line, recent neutron scattering experiments measure the dynamical spin susceptibility and find a feature at the nesting vector between electron and hole bands, located at an energy of 12.5 meV [31]. In our data we can identify a small shoulder in the quasiparticle interference at this energy [see Fig. 1(b)], although it seems quite adventurous to claim a strong relationship with neutron scattering experiments. In any event, the resonance in the dynamical spin susceptibility is actually quite broad and develops at low temperatures within the superconducting phase, so that we do not expect a clear signal in the quasiparticle interference of the hole bands. However, taken altogether, neutron scattering highlights the relevance of spin fluctuations, and available data showing sign changing superconductivity, including the data presented here and previous work [10,11,13], strongly

suggest that $\text{CaKFe}_4\text{As}_4$ is a $s \pm$ spin-fluctuation mediated superconductor.

Another interesting feature of $\text{CaKFe}_4\text{As}_4$ obtained from our data is that part of the hole bands reach their top at around 30–40 meV from the Fermi level. This resembles FeSe and related systems where the superconducting gap is practically of the same order as the position of the top of the hole bands [32,33]. In $\text{CaKFe}_4\text{As}_4$, the largest gap Δ_2 is close to 10 meV and the observed top of the band is several tens of meV above that value.

The band structure is likely influenced by small changes by doping. It would be interesting to search for doping induced modifications in the superconducting order parameter sign between the electron and hole bands. If the hole band can be brought closer to the Fermi level, predictions range from intraband $s \pm$ superconductivity to time-reversal symmetry breaking $s + is$ superconductivity, with superconducting order parameter phase differences among bands that are not multiples of π , due to the competition between Coulomb repulsion and spin fluctuations [20,34,35]. Furthermore, the presence of hedgehog spin vortex crystal in Ni doped $\text{CaKFe}_4\text{As}_4$, which is related to the absence of glide plane [12,34,36,37], adds an interesting ingredient likely favoring unconventional superconducting properties. Stoichiometric $\text{CaKFe}_4\text{As}_4$ is an advantageous starting point for exploring these ideas, compared with other iron based superconducting systems.

Let us note that there is no evidence for a significant in-plane anisotropy in $\text{CaKFe}_4\text{As}_4$. The situation is quite different from the fourfold gap anisotropy observed in LiFeAs or the strong twofold anisotropy in FeSe [38–40], but it is similar to the situation found in Fe-As based systems such as $\text{Ba}_{0.6}\text{K}_{0.4}\text{Fe}_2\text{As}_2$ [18,19,41].

Regarding the Caroli–de Gennes–Matricon vortex core bound states in $\text{CaKFe}_4\text{As}_4$, it is worth noting that we observe the lowest lying state at the center of the vortex core at a finite bias voltage, showing that electron-hole asymmetry is broken. This can be a consequence of having small values for $\Delta^2/2E_F$ and can be related to a low Fermi level E_F [42].

Electron-hole asymmetry at the center of vortex cores was observed previously in the nickel borocarbides, in cuprates, and in a number of pnictide systems [18,23,25,32,43–45]. Observations include peaks that are located at positive (electron) and at negative (hole) energies. In the pnictide superconductor LiFeAs , for instance, the amplitude is stronger for the hole side. In strained LiFeAs , the amplitude is higher in the electron side [46]. In $\text{Ba}_{0.6}\text{K}_{0.4}\text{Fe}_2\text{As}_2$ a peak is observed below the Fermi level, whereas in Co doped BaFe_2As_2 there is no zero bias peak, as this system is too close to the dirty limit, probably because of substitutional disorder [18,19,41]. In FeSe, the peak is at zero bias, and the vortex core is highly elongated, due to the nematic electronic anisotropy of this compound [32]. In $\text{FeTe}_{0.55}\text{Se}_{0.45}$, STM shows clear evidence of entering the quantum limit, with peaks appearing at nonzero energy at the centers of vortex cores [47]. From the gap values obtained in the tunneling density of states at zero magnetic field and the position in energy where they observe the peak at the center of vortex cores, the authors of [47] estimate a Fermi energy of a few meV. In some vortices, a single bound state is observed with large electron-hole asymmetry. The energies at which these bound states appear almost do not shift when moving

away from the vortex center, in agreement with theoretical calculations for the extreme quantum limit [42] (in pure 2H-NbSe₂, the peak shifts when moving away from the vortex center [22]). Also in agreement with these calculations are the observations of Friedel-like oscillations associated with these bound states. In some vortices, bound states appear at the same position in energy for positive and negative energies, but show asymmetry in the amplitudes. The origin of this electron-hole asymmetry is associated with the existence of shallow electron and hole bands, although disorder or defects might provide some influence too [44,47,48]. The actual influence of the band structure and of defects on the electron-hole symmetry of the Caroli–de Gennes–Matricon states is probably highly dependent on the details of each specific case.

In $\text{CaKFe}_4\text{As}_4$, we observe a single state with high amplitude for the electron side and located at about 0.4 meV. The peak does not show Friedel oscillations and its location in energy remains more or less at the same place when moving away from the vortex center (Fig. 3). We are thus well in the quantum limit, although the mean free path is probably lower than in other pnictide system, as discussed in the previous paragraph. From the position of the peak and the size of the superconducting gap, we can estimate Fermi energies of several tens of meV, an order of magnitude above the results obtained in $\text{FeTe}_{0.55}\text{Se}_{0.45}$ [47]. It is tempting to associate the electron-hole asymmetry with the β band reaching its top at a similar energy scale, although this requires calculations of the core levels using the band structure of $\text{CaKFe}_4\text{As}_4$ and taking into account the influence of defects.

The vortex core size provides a well defined length scale within the mixed state. One can consider if the different gap magnitudes lead to different length scales in the spatial variation of the order parameter around the vortex core. The difference between gap magnitudes is large in $\text{CaKFe}_4\text{As}_4$. Our experiments show that there is a single length scale. The range of interband coupling parameters where different length scales might appear in the spatial variation of the order parameter has been predicted to be small [49] and quite difficult to reach in real systems [50].

Finally, let us discuss the disorder in the vortex lattice. Disordered vortex lattices have been observed by STM in several iron based superconductors. Experiments on doped compounds report varied behavior. Vortex lattice images of $(\text{Sr}_{0.75}\text{K}_{0.25})\text{Fe}_2\text{As}_2$ [51] and $\text{Ba}(\text{Fe}_{0.9}\text{Co}_{0.1})_2\text{As}_2$ [41] show a disordered vortex lattice while $(\text{Ba}_{0.6}\text{K}_{0.4})\text{Fe}_2\text{As}_2$ [18] presents a more ordered lattice for the same values of the magnetic fields. This indicates that charge doping by itself does not explain the origin of vortex pinning in these materials. Instead, it has been suggested that electronic inhomogeneity induced by ion size mismatch between substituted elements accounts for the different pinning strengths found in these compounds (for instance, the mismatch between K and Ba is five times smaller than between K and Sr) [51]. In bulk $\text{Fe}(\text{Se},\text{Te})$ irradiated by heavy ions, vortices are pinned to the amorphous regions at the columnar defects created by irradiation, leading to a complicated pinning landscape [52]. In FeSe, vortices are preferentially positioned near twin boundaries where superconductivity is strongly suppressed [53]. In the stoichiometric pnictide LiFeAs a very disordered vortex lattice has been observed in absence of twin boundaries or

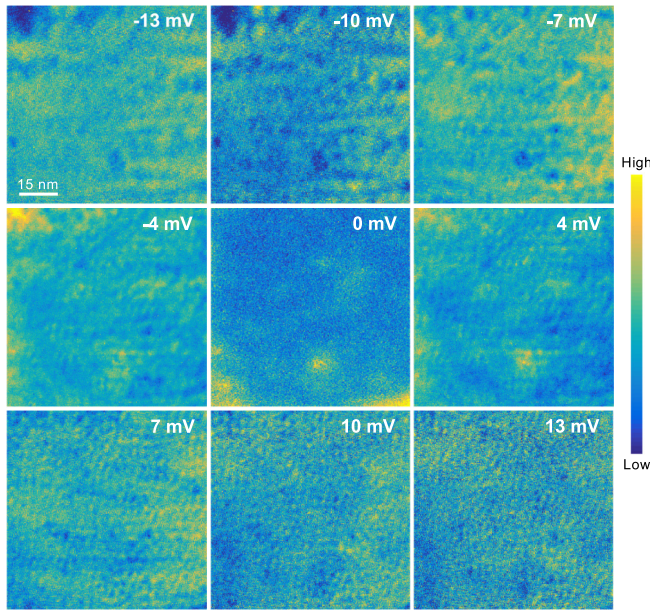


FIG. 4. Conductance maps as a function of energy showing the evolution of the QPI pattern analyzed in Fig. 1.

substitutional disorder but at much larger values of H/H_{c2} , for which vortex disorder due to lattice softening is much more significant than here [38]. The present results in stoichiometric $\text{CaKFe}_4\text{As}_4$ uniquely show the link between the locations with a finite density of states at the Fermi level and the vortex positions. Our experiment shows that the disordered vortex lattice characteristic of FeBSC superconductors is due to order parameter suppression at defects whose size is of the order of the vortex core size.

In summary, we provide a comprehensive study including band structure and vortex lattice measurements of the newly found high- T_c stoichiometric $\text{CaKFe}_4\text{As}_4$. We show that there is a strong relationship between gap structure, vortex cores, and vortex pinning due to the intrinsic properties of FeBSC, namely $s \pm$ superconductivity and a set of highly dispersive bands close to the Fermi level.

ACKNOWLEDGMENTS

We acknowledge discussions with R. Prozorov and S. Vieira. Work done in Madrid (A.F., I.G. and H.S.) was supported by the Spanish State Agency for Research, AEI

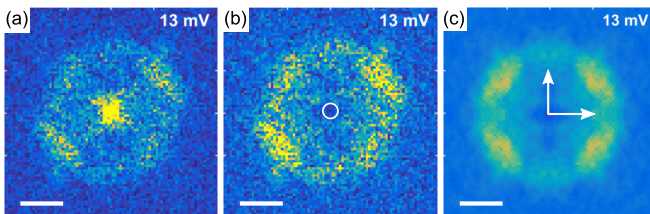


FIG. 5. In (a) we show the raw Fourier transform of our conductance map at 13 mV. In (b) we have removed the central circle marked in white symbol. In (c) we show the result of a Gaussian smoothing to (b). The white scale bar in FFT is $0.1\pi/a$ long.

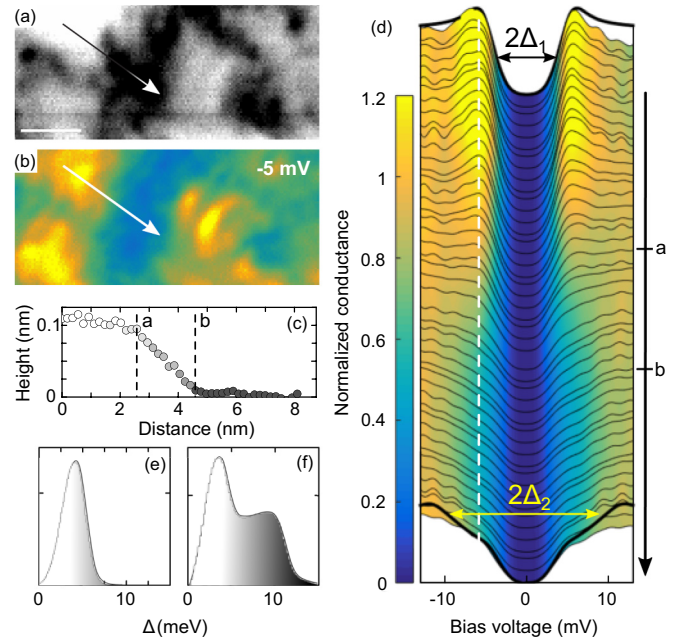


FIG. 6. (a) STM topography of an almost atomically flat area. The difference between black and white is given by the height profile in (c) along the arrow. The white scale bar is 4 nm long. (b) Represents the normalized tunneling conductance over the area in (a) taken at -5 mV. The image shows a clear relation between the gap structure and the part of the surface in which we are tunneling. (c) Height profile along the line scan shown in (a). (d) Normalized conductance curves taken along the arrows in (a) and (b). We mark by arrows the main values of the superconducting gap found, as discussed in the text, Δ_1 and Δ_2 . The white dashed line is a guide to the eye. The dark arrow on the right and labels “a” and “b” refer to positions shown in (c). (e) and (f) Distribution of gap values Δ being the gap values and the relative weight of the corresponding gap values γ . Using the distributions shown in the figure, we generate a superconducting density of states summing over all gaps with the corresponding weights (see text). We convolute the resulting density of states with the derivative of the Fermi function to find the tunneling conductance given by the black lines at the top and bottom of the panel in (d).

(FIS2014-54498-R, MDM-2014-0377), by the Comunidad de Madrid through program Nanofrontmag-CM (S2013/MIT-2850), by the European Research Council PNICTEYES Grant Agreement No. 679080 (IG) and by FP7-PEOPLE-2013-CIG 618321, Cost CA16218 Nanocohybi, and Axa Research Fund. SEGAINVEX-UAM and Banco Santander are also acknowledged. Work done in Ames Lab (P.C.C., S.L.B., V.G.K., W.R.M., and T.K.) was supported by the US Department of Energy, Office of Basic Energy Science, Division of Materials Sciences and Engineering. Ames Laboratory is operated for the US Department of Energy by Iowa State University under Contract No. DE-AC02-07CH11358. W.R.M. was supported by the Gordon and Betty Moore Foundation’s EPIQS Initiative through Grant No. GBMF4411.

APPENDIX

1. Quasiparticle interference and symmetrization

We present in Fig. 4 a representative set of the real space conductance maps of our quasiparticle interference

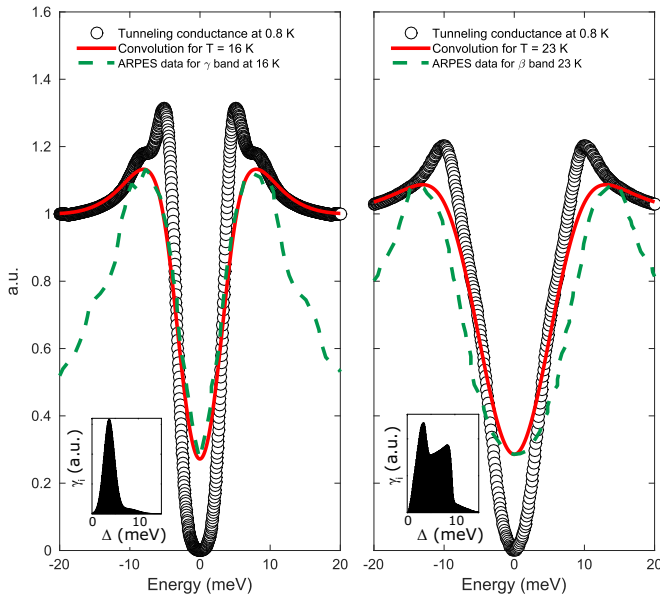


FIG. 7. Tunneling conductance data (open symbols) compared with ARPES data (green lines) from Ref. [11]. We compare our data with ARPES at the β band (left panel) and at the γ band (right panel). Data from ARPES are in arbitrary units (y axis) and tunneling data are normalized to 1 at 20 mV. The left panel includes data taken from the white colored areas of Fig. 6(a) [yellow in Fig. 6(b)] and the right panel data are from the dark areas in Fig. 6(a) [blue in Fig. 6(b)]. Insets show the gap distributions corresponding to each conductance curve, as in Figs. 6(e) and 6(f). ARPES data are taken at 16 K, whereas tunneling conductance is taken at 0.8 K. Red lines represent the tunneling conductance convoluted with the temperature smearing corresponding to 16 K.

experiments. Background modulation evolves with energy producing the reciprocal space images seen in the left panel of Fig. 1. No modulation is seen for energy values inside the superconducting gap.

In Fig. 5 we show the process followed to obtain the Fourier transform of the tunneling conductance maps. We discuss the Fourier transform of the map at 13 mV as a representative example. In Fig. 5(a) we show the Fourier transform of raw data. In Fig. 5(b) we remove the central peak and in Fig. 5(c) we show the result of the symmetrization. The raw data show some asymmetry due to spatial structure of defects. The symmetry of the in-plane lattice is expected to be $4mm$. However, we decided to apply a $2mm$ symmetrization. This leaves part of the asymmetry due to anisotropic defect scattering, but the figures are more clear and it provides a representation closer to the raw data. In any event, this does not influence the results, which focus on the bias voltage dependence of the radial average of the intensity of the quasiparticle pattern along the path marked by a white dashed line, which corresponds to the circle of maximum intensity in Fig. 1.

2. Tunneling conductance vs position in different tunneling planes

In Fig. 6 we show tunneling spectroscopy in a very small and flat area. We obtain tunneling conductance curves with two characteristic gap values, $\Delta_1 = 3 \text{ meV} = 0.6\Delta_0$ and

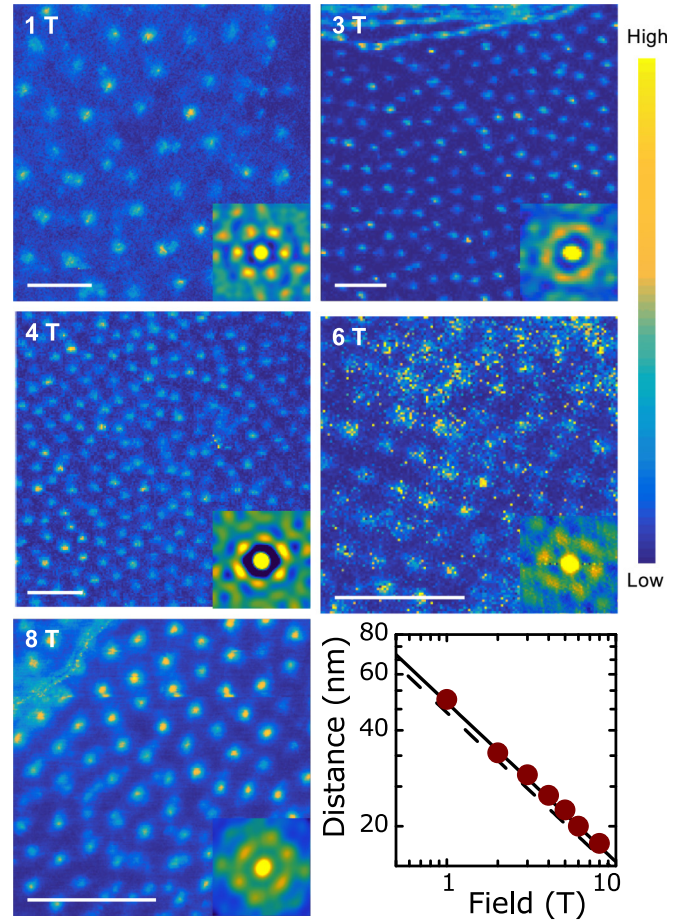


FIG. 8. Zero bias conductance maps in fields of view between 1 and 8 T taken at different positions. The color bar on the right provides the zero bias normalized tunneling conductance. The white bar in the images is of 82 nm size. The insets in the images show the autocorrelations function of the images. Note that the lattice remains hexagonal, within first nearest neighbors, over the whole magnetic field range. The lower right panel shows the intervortex distance, obtained from the autocorrelation function, vs the magnetic field, and the black lines are the expected intervortex distance for hexagonal (solid line) and square (dashed line) lattices, corresponding to $a_0 \propto \frac{1}{\sqrt{H}}$.

$\Delta_2 = 8 \text{ meV} = 1.5\Delta_0$ (with $\Delta_0 = 1.76k_B T_c$). To determine these values, we calculate the tunneling conductance assuming a density of states of the form $\sum_{\Delta_i} \gamma_i \text{Re}(\sqrt{\frac{E}{E^2 - \Delta_i^2}})$ and convolute the result with the derivative of the Fermi function to include the effect of temperature. Δ_1 and Δ_2 are the peaks thus obtained in the distribution of weights γ_i . The gap values we obtain agree with previous STM and penetration depth experiments [10,11]. The weight of Δ_1 and Δ_2 in the tunneling conductance changes when crossing a stripe, leading to different distribution of γ_i [Figs. 6(e) and 6(f)]. The contribution of different parts of the Fermi surface to the tunneling conductance changes as a function of the atomic plane into which we are tunneling, because in each surface the tunneling matrix elements, linked to the terminating surface atoms, are different [18,19,24]. Very similar results are obtained in $(\text{Ba}_{1-x}\text{K}_x)\text{Fe}_2\text{As}_2$ [18].

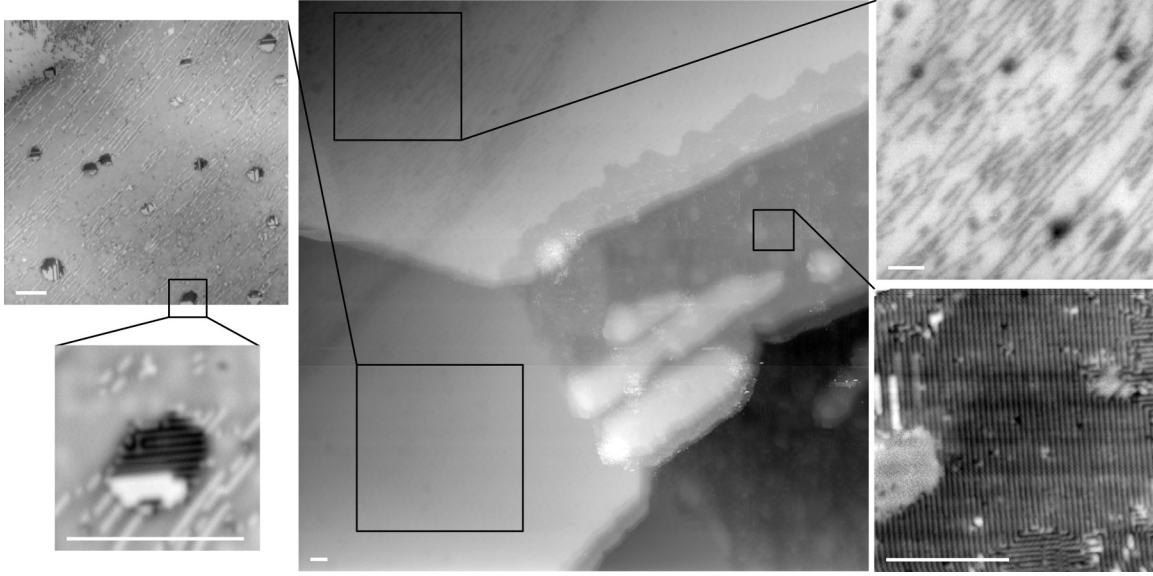


FIG. 9. Features of the surface topography measured by STM in $\text{CaKFe}_4\text{As}_4$. Scale is given by the white bars in every panel, of 20 nm size. The main panel shows a large area with different surfaces (5.6 nm change in height from black to white). The upper right and upper left panels provide a zoom on two of these surfaces. These are most frequently observed. The top left image shows a contrast from black to white of 0.85 nm. The top right image spans 0.3 nm. In the top left image, we make an additional zoom into a small hole like defect. The height difference in this image (from white to black) is 0.5 nm, that is, of just two atoms. The bottom right image is a zoom on an area where we observe a surface reconstruction. This is rarely observed on the surface of the sample.

It is also useful to compare the results of the tunneling conductance with previous ARPES experiments (see Fig. 7). We see that the small sized gap observe in tunneling coincides with the gap in the β band and the larger gap with the gap in the γ band obtained in ARPES [11].

3. Obtaining the vortex core radius \mathcal{C}

To obtain the magnetic field dependence of the vortex core radius \mathcal{C} , we take zero bias conductance maps of vortices that have a round shape and are far from pinning centers. We then center the image at a single vortex and make the angular average of the tunneling conductance for each distance r from the vortex center. We define the normalized conductance as

$$\sigma = \frac{\sigma_0(r) - \sigma_0(r^*)}{\sigma_0(0) - \sigma_0(r^*)}, \quad (\text{A1})$$

where σ is the normalized conductance shown in the Fig. 2(c), σ_0 the angular average over the center of the vortex in a tunneling conductance map, and r the distance from the vortex center. r^* is the distance from the vortex center to the center of a vortex triangle, or the size of the Wigner-Seitz cell of the vortex lattice. This is also the normalization parameter used in Fig. 2(c). Further details are given in Ref. [28].

4. Vortex lattice at different fields

Figure 8 contains zero bias conductance maps taken in different areas at different fields between 1 and 8 T. The corresponding autocorrelation function is included as an inset in each map. It shows sixfold features as expected within a triangular lattice with disorder. The magnetic field dependence of the intervortex distance a_0 follows expectations for a

triangular vortex lattice (solid line), $a_0^2 = 2\Phi_0/\sqrt{3}H$ (where Φ_0 is the flux quantum).

Figure 8 also shows how vortex position follow pair breaking defects. See for example the 3 T image, where the vortices align following a curved line with a finite zero bias conductance in between vortices going from the top left part to the center of the image.

5. Atomic scale features in the surface of $\text{CaKFe}_4\text{As}_4$

As discussed above, the crystal structure of $\text{CaKFe}_4\text{As}_4$ has relevant differences from CaFe_2As_2 , such as the absence of a glide plane and the positions of the Fe-As layers. However, they are both tetragonal phases with quite similar atomic positions in them [8]. It is, therefore, reasonable to assume that the cleaving in $\text{CaKFe}_4\text{As}_4$ occurs next to Fe-As blocks as happens in CaFe_2As_2 and its doped compounds. These often show a 2×1 surface reconstruction consisting of rows of Ca atoms that remain on the surface after cleaving [14,18,19,54]. We do not observe such a reconstruction in the surfaces of $\text{CaKFe}_4\text{As}_4$ over large areas. Such surfaces are very rare, and therein we see no superconducting features in the tunneling conductance. The notable stress sensitivity of CaFe_2As_2 is attributed to the small size of the Ca ions. The different size and regular order of Ca and K may mitigate these steric effects in $\text{CaKFe}_4\text{As}_4$ [55].

In Fig. 9 we show a large area which is useful to discuss the atomic size features of the surface of $\text{CaKFe}_4\text{As}_4$ and relate these to previous findings in Fe based superconductors.

The zooms in the upper left and right panels provide the typical images found at the surface of $\text{CaKFe}_4\text{As}_4$. Within the same image we also show a large area with a surface reconstruction (bottom right panel of Fig. 9). These surfaces

are extremely rare. The most common surfaces are flat down to fractions of a nm with, however, no visible atomic lattice on them. Instead, we observe small stripes as shown in upper left and right panels of Fig. 9. These areas are interspersed with small point size defects that provide the quasiparticle

scattering discussed in Fig. 1. The stripe like features are possibly missing rows of alkali (K) and alkaline-earth (Ca) atoms. The stripes and the internal shape of the defects give the oscillations discussed above [Figs. 1(e) and 1(f)], and provide the anisotropy for the scattering potential $|V_s(\vec{q})|^2$.

-
- [1] Y. Kamihara, T. Watanabe, M. Hirano, and H. Hosono, Iron-based layered superconductor $\text{La}[\text{O}_{1-x}\text{F}_x]\text{FeAs}$ ($x = 0.05\text{--}0.12$) with $T_c = 26$ K, *J. Am. Chem. Soc.* **130**, 3296 (2008).
- [2] P. C. Canfield and S. L. Bud'ko, FeAs-based superconductivity: A case study of the effects of transition metal doping on BaFe_2As_2 , *Annu. Rev. Condens. Matter Phys.* **1**, 27 (2010).
- [3] J. Paglione and R. L. Greene, Manifesto for a higher T_c , *Nat. Phys.* **6**, 645 (2010).
- [4] P. J. Hirschfeld, M. M. Korshunov, and I. I. Mazin, Gap symmetry and structure of Fe-based superconductors, *Rep. Prog. Phys.* **74**, 124508 (2011).
- [5] D. V. Efremov, M. M. Korshunov, O. V. Dolgov, A. A. Golubov, and P. J. Hirschfeld, Disorder-induced transition between s_{\pm} and s_{++} states in two-band superconductors, *Phys. Rev. B* **84**, 180512 (2011).
- [6] H. Hosono and K. Kuroki, Iron-based superconductors: Current status of materials and pairing mechanism, *Physica C* **514**, 399 (2015).
- [7] A. Iyo, K. Kawashima, T. Kinjo, T. Nishio, S. Ishida, H. Fujihisa, Y. Gotoh, K. Kihou, H. Eisaki, and Y. Yoshida, New-structure-type Fe-based superconductors: $\text{CaAFe}_4\text{As}_4$ ($A = \text{K}, \text{Rb}, \text{Cs}$) and $\text{SrAFe}_4\text{As}_4$ ($A = \text{Rb}, \text{Cs}$), *J. Am. Chem. Soc.* **138**, 3410 (2016).
- [8] W. R. Meier, T. Kong, U. S. Kaluarachchi, V. Taufour, N. H. Jo, G. Drachuck, A. E. Böhmer, S. M. Saunders, A. Sapkota, A. Kreyssig, M. A. Tanatar, R. Prozorov, A. I. Goldman, F. F. Balakirev, A. Gurevich, S. L. Bud'ko, and P. C. Canfield, Anisotropic thermodynamic and transport properties of single-crystalline $\text{CaKFe}_4\text{As}_4$, *Phys. Rev. B* **94**, 064501 (2016).
- [9] A. E. Böhmer, A. Sapkota, A. Kreyssig, S. L. Bud'ko, G. Drachuck, S. M. Saunders, A. I. Goldman, and P. C. Canfield, Effect of Biaxial Strain on the Phase Transitions of $\text{Ca}(\text{Fe}_{1-x}\text{Co}_x)_2\text{As}_2$, *Phys. Rev. Lett.* **118**, 107002 (2017).
- [10] K. Cho, A. Fente, S. Teknowijoyo, M. A. Tanatar, K. R. Joshi, N. M. Nusran, T. Kong, W. R. Meier, U. S. Kaluarachchi, I. Guillamón, H. Suderow, S. L. Bud'ko, P. C. Canfield, and R. Prozorov, Nodeless multiband superconductivity in stoichiometric single-crystalline $\text{CaKFe}_4\text{As}_4$, *Phys. Rev. B* **95**, 100502 (2017).
- [11] D. Mou, T. Kong, W. R. Meier, F. Lochner, L.-L. Wang, Q. Lin, Y. Wu, S. L. Bud'ko, I. Eremin, D. D. Johnson, P. C. Canfield, and A. Kaminski, Enhancement of the Superconducting Gap by Nesting in $\text{CaKFe}_4\text{As}_4$: A New High Temperature Superconductor, *Phys. Rev. Lett.* **117**, 277001 (2016).
- [12] W. R. Meier, Q.-P. Ding, A. Kreyssig, S. L. Bud'ko, A. Sapkota, K. Kothapalli, V. Borisov, R. Valentí, C. D. Batista, P. P. Orth, R. M. Fernandes, A. I. Goldman, Y. Furukawa, A. E. Böhmer, and P. C. Canfield, Hedgehog spin-vortex crystal stabilized in a hole-doped iron-based superconductor, *NPJ Quant. Mater.* **3**, 5 (2018).
- [13] J. Cui, Q. P. Ding, W. R. Meier, A. E. Böhmer, T. Kong, V. Borisov, Y. Lee, S. L. Bud'ko, R. Valentí, P. C. Canfield, and Y. Furukawa, Magnetic fluctuations and superconducting properties of $\text{CaKFe}_4\text{As}_4$ studied by ^{75}As NMR, *Phys. Rev. B* **96**, 104512 (2017).
- [14] A. Fente, A. Correa-Orellana, A. E. Böhmer, A. Kreyssig, S. Ran, S. L. Bud'ko, P. C. Canfield, F. J. Mompean, M. García-Hernández, C. Munuera, I. Guillamón, and H. Suderow, Direct visualization of phase separation between superconducting and nematic domains in Co-doped CaFe_2As_2 close to a first order phase transition, *Phys. Rev. B* **97**, 014505 (2018).
- [15] W. R. Meier, T. Kong, S. L. Bud'ko, and P. C. Canfield, Optimization of the crystal growth of the superconductor $\text{CaKFe}_4\text{As}_4$ from solution in the $\text{FeAs}\text{--}\text{CaFe}_2\text{As}_2\text{--}\text{KFe}_2\text{As}_2$ system, *Phys. Rev. Mater.* **1**, 013401 (2017).
- [16] H. Suderow, I. Guillamón, and S. Vieira, Compact very low temperature scanning tunneling microscope with mechanically driven horizontal linear positioning stage, *Rev. Sci. Instrum.* **82**, 033711 (2011).
- [17] J. G. Rodrigo, H. Suderow, S. Vieira, E. Bascones, and F. Guinea, Superconducting nanostructures fabricated with the scanning tunnelling microscope, *J. Phys.: Condens. Matter* **16**, R1151 (2004).
- [18] L. Shan, Y. L. Wang, B. Shen, B. Zeng, Y. Huang, A. Li, D. Wang, H. Yang, C. Ren, Q. H. Wang, S. H. Pan, and H. H. Wen, Observation of ordered vortices with Andreev bound states in $\text{Ba}_{0.6}\text{K}_{0.4}\text{Fe}_2\text{As}_2$, *Nat. Phys.* **7**, 325 (2011).
- [19] J. E. Hoffman, Spectroscopic scanning tunneling microscopy insights into Fe-based superconductors, *Rep. Prog. Phys.* **74**, 124513 (2011).
- [20] P. J. Hirschfeld, Using gap symmetry and structure to reveal the pairing mechanism in Fe-based superconductors, *C. R. Phys.* **17**, 197 (2016).
- [21] C. Caroli, P. G. De Gennes, and J. Matricon, Bound Fermion States on a Vortex Line in a Type II Superconductor, *Phys. Lett.* **9**, 307 (1964).
- [22] H. F. Hess, R. B. Robinson, and J. V. Waszczak, Vortex-Core Structure Observed with a Scanning Tunneling Microscope, *Phys. Rev. Lett.* **64**, 2711 (1990).
- [23] Ø. Fischer, M. Kugler, I. Maggio-Aprile, C. Berthod, and C. Renner, Scanning tunneling spectroscopy of high-temperature superconductors, *Rev. Mod. Phys.* **79**, 353 (2007).
- [24] H. Suderow, I. Guillamón, J. G. Rodrigo, and S. Vieira, Imaging superconducting vortex cores and lattices with a scanning tunneling microscope, *Supercond. Sci. Technol.* **27**, 063001 (2014).
- [25] N. Hayashi, M. Ichioka, and K. Machida, Star-Shaped Local Density of States Around Vortices in a Type-II Superconductor, *Phys. Rev. Lett.* **77**, 4074 (1996).
- [26] I. Guillamón, H. Suderow, F. Guinea, and S. Vieira, Intrinsic atomic-scale modulations of the superconducting gap of 2H-NbSe_2 , *Phys. Rev. B* **77**, 134505 (2008).

- [27] I. Guillamón, H. Suderow, S. Vieira, L. Cario, P. Diener, and P. Rodière, Superconducting Density of States and Vortex Cores of 2H-NbSe₂, *Phys. Rev. Lett.* **101**, 166407 (2008).
- [28] A. Fente, E. Herrera, I. Guillamón, H. Suderow, S. Mañas-Valero, M. Galbiati, E. Coronado, and V. G. Kogan, Field dependence of the vortex core size probed by scanning tunneling microscopy, *Phys. Rev. B* **94**, 014517 (2016).
- [29] G. Blatter, M. V. Feigel'man, V. B. Geshkenbein, A. I. Larkin, and V. M. Vinokur, Vortices in high-temperature superconductors, *Rev. Mod. Phys.* **66**, 1125 (1994).
- [30] F. Lochner, F. Ahn, T. Hickel, and I. Eremin, Electronic properties, low-energy Hamiltonian, and superconducting instabilities in CaKFe₄As₄, *Phys. Rev. B* **96**, 094521 (2017).
- [31] K. Iida, M. Ishikado, Y. Nagai, H. Yoshida, A. D. Christianson, N. Murai, K. Kawashima, Y. Yoshida, H. Eisaki, and A. Iyo, Spin resonance in the new-structure-type iron-based superconductor CaKFe₄As₄, *J. Phys. Soc. Jpn.* **86**, 093703 (2017).
- [32] S. Kasahara, T. Watashige, T. Hanaguri, Y. Kohsaka, T. Yamashita, Y. Shimoyama, Y. Mizukami, R. Endo, H. Ikeda, K. Aoyama, T. Terashima, S. Uji, T. Wolf, H. von Löhneysen, T. Shibauchi, and Y. Matsuda, Field-induced superconducting phase of FeSe in the BCS-BEC crossover, *Proc. Natl. Acad. Sci. USA* **111**, 16309 (2014), <http://www.pnas.org/content/111/46/16309.full.pdf>.
- [33] K. Okazaki, Y. Ito, Y. Ota, Y. Kotani, T. Shimojima, T. Kiss, S. Watanabe, C.-T. Chen, S. Niitaka, T. Hanaguri, H. Takagi, A. Chainani, and S. Shin, Superconductivity in an electron band just above the Fermi level: Possible route to BCS-BEC superconductivity, *Sci. Rep.* **4**, 4109 (2014).
- [34] J. Böker, P. A. Volkov, K. B. Efetov, and I. Eremin, $s + is$, *Phys. Rev. B* **96**, 014517 (2017).
- [35] Y. Wang, T. Berlijn, P. J. Hirschfeld, D. J. Scalapino, and T. A. Maier, Glide-Plane Symmetry and Superconducting Gap Structure of Iron-Based Superconductors, *Phys. Rev. Lett.* **114**, 107002 (2015).
- [36] J. O'Halloran, D. F. Agterberg, M. X. Chen, and M. Weinert, Stabilizing the spin vortex crystal phase in two-dimensional iron-based superconductors, *Phys. Rev. B* **95**, 075104 (2017).
- [37] R. M. Fernandes, S. A. Kivelson, and E. Berg, Vestigial chiral and charge orders from bidirectional spin-density waves: Application to the iron-based superconductors, *Phys. Rev. B* **93**, 014511 (2016).
- [38] T. Hanaguri, K. Kitagawa, K. Matsubayashi, Y. Mazaki, Y. Uwatoko, and H. Takagi, Scanning tunneling microscopy/spectroscopy of vortices in LiFeAs, *Phys. Rev. B* **85**, 214505 (2012).
- [39] Y. Wang, P. J. Hirschfeld, and I. Vekhter, Theory of quasiparticle vortex bound states in iron-based superconductors: Application to scanning tunneling spectroscopy of LiFeAs, *Phys. Rev. B* **85**, 020506 (2012).
- [40] C.-L. Song, Y.-L. Wang, P. Cheng, Y.-P. Jiang, W. Li, T. Zhang, Z. Li, K. He, L. Wang, J.-F. Jia, H.-H. Hung, C. Wu, X. Ma, X. Chen, and Q.-K. Xue, Direct observation of nodes and twofold symmetry in FeSe superconductor, *Science* **332**, 1410 (2011).
- [41] Y. Yin, M. Zech, T. L. Williams, X. F. Wang, G. Wu, X. H. Chen, and J. E. Hoffman, Scanning Tunneling Spectroscopy and Vortex Imaging in the Iron Pnictide Superconductor BaFe_{1.8}Co_{0.2}As₂, *Phys. Rev. Lett.* **102**, 097002 (2009).
- [42] N. Hayashi, T. Isoshima, M. Ichioka, and K. Machida, Low-Lying Quasiparticle Excitations Around a Vortex Core in Quantum Limit, *Phys. Rev. Lett.* **80**, 2921 (1998).
- [43] Sh.-ic. Kaneko, K. Matsuba, M. Hafiz, K. Yamasaki, E. Kakizaki, N. Nishida, H. Takeya, K. Hirata, T. Kawakami, T. Mizushima, and K. Machida, Quantum limiting behaviors of a vortex core in an anisotropic gap superconductor, *J. Phys. Soc. Jpn.* **81**, 063701 (2012).
- [44] C. Berthod, Vortex spectroscopy in the vortex glass: A real-space numerical approach, *Phys. Rev. B* **94**, 184510 (2016).
- [45] H. Nishimori, K. Uchiyama, S. Kaneko, A. Tokura, H. Takeya, K. Hirata, and N. Nishida, First observation of the fourfold-symmetric and quantum regime vortex core in YNi₂B₂C by scanning tunneling microscopy and spectroscopy, *J. Phys. Soc. Jpn.* **73**, 3247 (2004).
- [46] C. M. Yim, C. Trainer, R. Aluru, S. Chi, W. N. Hardy, R. Liang, D. Bonn, and P. Wahl, Discovery of a strain-stabilised charge density wave in LiFeAs, [arXiv:1802.05019](https://arxiv.org/abs/1802.05019).
- [47] M. Chen, X. Chen, H. Yang, Z. Du, X. Zhu, E. Wang, and H.-H. Wen, Discrete energy levels of Caroli-de Gennes-Martricon states in quantum limit due to small Fermi energy in FeTe_{0.55}Se_{0.45}, [arXiv:1709.09401](https://arxiv.org/abs/1709.09401).
- [48] Q. Han, L.-y. Zhang, and Z. D. Wang, Effect of a point impurity on the vortex bound states in an s-wave superconductor: A self-consistent analysis, *Phys. Rev. B* **62**, 5936 (2000).
- [49] M. Silaev and E. Babaev, *Phys. Rev. B* **85**, 134514 (2012).
- [50] M. Ichioka, V. G. Kogan, and J. Schmalian, Locking of length scales in two-band superconductors, *Phys. Rev. B* **95**, 064512 (2017).
- [51] C.-L. Song, Y. Yin, M. Zech, T. Williams, M. M. Yee, G.-F. Chen, J.-L. Luo, N.-L. Wang, E. W. Hudson, and J. E. Hoffman, Dopant clustering, electronic inhomogeneity, and vortex pinning in iron-based superconductors, *Phys. Rev. B* **87**, 214519 (2013).
- [52] F. Massee, P. O. Sprau, Y.-L. Wang, J. C. S. Davis, G. Ghigo, G. D. Gu, and W.-K. Kwok, Imaging atomic-scale effects of high-energy ion irradiation on superconductivity and vortex pinning in Fe(Se,Te), *Sci. Adv.* **1**, e1500033 (2015).
- [53] C.-L. Song, Y.-L. Wang, Y.-P. Jiang, L. Wang, K. He, X. Chen, J. E. Hoffman, X.-C. Ma, and Q.-K. Xue, Suppression of Superconductivity by Twin Boundaries in FeSe, *Phys. Rev. Lett.* **109**, 137004 (2012).
- [54] F. Massee, Y. Huang, R. Huisman, S. de Jong, J. B. Goedkoop, and M. S. Golden, Nanoscale superconducting-gap variations and lack of phase separation in optimally doped BaFe_{1.86}Co_{0.14}As₂, *Phys. Rev. B* **79**, 220517 (2009).
- [55] S. Ran, S. L. Bud'ko, D. K. Pratt, A. Kreyssig, M. G. Kim, M. J. Kramer, D. H. Ryan, W. N. Rowan-Weetaluktuk, Y. Furukawa, B. Roy, A. I. Goldman, and P. C. Canfield, Stabilization of an ambient-pressure collapsed tetragonal phase in CaFe₂As₂ and tuning of the orthorhombic-antiferromagnetic transition temperature by over 70 K via control of nanoscale precipitates, *Phys. Rev. B* **83**, 144517 (2011).